pp. 1–25 (2020)

Analysis of the impact of left ventricular assist devices on the systemic circulation

S. S. Simakov[*†], A. E. Timofeev[*], T. M. Gamilov[*†], P. Yu. Kopylov[†], D. V. Telyshev[†‡], and Yu. V. Vassilevski[*†§]

Abstract — In this work we analyze the impact of left ventricular assist devices on the systemic circulation in subjects with heart failure associated with left ventricular dilated cardiomyopathy. We use an integrated model of the left heart and blood flow in the systemic arteries with a left ventricular assist device. We study the impact of the rotation speed of the pump on haemodynamic characteristics of distal arteries. We identify the rotation speed for simultaneous recovery of the healthy average values in all systemic arteries, the heart and the aorta. Our numerical experiments show that blood distribution over the graph of systemic vessels does not depend on flow regimes in ascending aorta. We also observe that the optimal pump rotation speed changes in the atherosclerotic vascular network and depends on stenoses localization.

Keywords: Left ventricular assist device, lumped model, cardiac dynamics, haemodynamics, aortic valve, atherosclerosis

MSC 2010: 65D25, 37M05, 92B99

The usage of left ventricular assist devices (LVADs) is a therapeutic option for patients with end-stage heart failure (HF). LVAD connects the left ventricle (LV) and the aortic arch (AA) and provides a long term circulatory support as a bridge to the heart transplantation or as an alternative treatment of HF. Modern LVADs are rotary blood pumps which produce continuous flow [17, 26]. The total inflow to the aorta is the sum of the LV and LVAD outflows. The primary goal of LVAD is to maintain haemodynamic conditions for sufficient oxygen and nutrients delivery to patient's organs and tissues. The outflow from LVAD to the aorta depends on many factors: the pulmonary pressure, LV contraction and ejection, aortic valve (AV) function,

[*]Moscow Institute of Physics and Technology, Dolgoprudny 141701, Moscow Region, Russia
E-mail: richardstallman42@gmail.com

[†]Sechenov University, Moscow 119991, Russia

[‡]National Research University of Electronic Technology, Zelenograd 124498, Bld. 5, Pas. 4806, Russia

[§]Marchuk Institute of Numerical Mathematics of the Russian Academy of Sciences, Moscow 119333, Russia

The research was supported by the Russian Foundation for Basic Research (grant Nos. 18-00-01661, 18-00-01524, 18-00-01659, 18-31-20048, 19-51-45001) and the world-class research center 'Moscow Center for Fundamental and Applied Mathematics' (agreement with the Ministry of Education and Science of the Russian Federation No. 075-15-2019-1624).

aorta extensibility and peripheral conditions in distal systemic arteries. Also, the rotation speed of the pump rotor is a parameter which controls the pump operation. These and other parameters influence the pressure drop across LVAD and thus contribute to the LVAD outflow.

Efficacy of LVAD has been proven [48], although the impact of LVAD on the blood circulation is not always clear. Efficient autonomous control of LVAD rotation speed taking into account physical load, concomitant diseases and other individual cardiovascular conditions is still the open question. Mechanical performance of LVADs in different regimes is studied on mock circulation facilities for adult and paediatric conditions [29, 46, 47]. However, these experimental tools are not individualized and provide limited information. Mathematical modelling of the cardiovascular system with installed LVAD is a powerful instrument of such studies. It is used in FSI simulations of blood flow near the heart valves after LVAD implantation [30], analysis of coronary perfusion and ventricular afterload [22], simulation of the LVAD impact on adult and paediatric haemodynamics by lumped closed-loop models [37], analysis of various control strategies [9,28], patient-specific CFD simulations of LVAD impact and embolisation rate in cerebral vessels [3]. To the best of our knowledge, the detailed analysis of the LVAD impact on the blood flow in the systemic arteries has not been performed yet.

In this work we use an integrated *in silico* model of the left heart with LVAD and a 1D network haemodynamic model in systemic arteries. Our primary goal is to analyze performance of LVADs Sputnik 2 and Sputnik D [29, 35, 46, 47, 49] in realistic physiological conditions. We also compare models of the Sputnik devices with a reference model of the HeartMate II [6], the well known and widely used pump. To this end, we reconsider a heart model accounting heart failure (HF) associated with the LV dilated cardiomyopathy (DCM) and possible presence of LVAD and determine the optimal rotation speed which recovers the normal average values of flow, pressure and velocity in the systemic arteries.

The paper is organized as follows. In Section 1 of this work we present an integrated model of the left heart function with opening/closing of the aortic valve (AV) and the mitral valve (MV) and a 1D network model of blood flow in systemic arteries closed by Windkessel compartments as outflow conditions. The LVAD model is included in the integrated model as a nonlinear lumped compartment which connects the LV and the AA. The LVAD model for pumps Sputnik 2 and Sputnik D was validated in [42] by fitting its parameters with measurements at mock circulation facilities. Parameters of the LVAD model for pump HeartMate II are taken from [6]. Thus we extend our previous model [42] which includes the left heart function, the LVAD and two segments of aorta closed by a single Windkessel compartment.

In Section 2 we discuss performance of the integrated model in pathological conditions. In Section 2.1 we study the impact of the LVADs on the systemic circulation in case of HF accompanied by LV DCM. In Section 2.2 we study the blood flow in coronary, cerebral and leg arteries in the presence of atherosclerosis and installed LVAD. The optimal pump rotation speed turns to be sensitive to stenoses localization. Our results with the integrated 1D network model of the systemic circu-

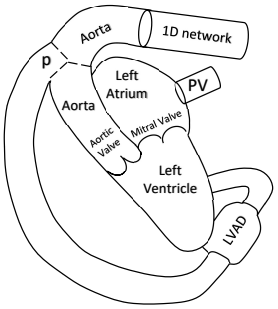

Figure 1. Scheme of LVAD installation.

lation confirm our previous findings with the reduced 1D model of aorta represented by two segments [42] with a single Windkessel compartment. Thus, the current and the previous models are equivalent in terms of haemodynamic characteristics of the heart and the aorta. Using the extended model we found that none of the pumps is capable to recover simultaneously the normal average values in the heart and the aorta (in the ranges recommended by the manufacturers) and to comply with all criteria of physiologically feasible operation. We identify the rotation speed for recovery of the normal average values in all systemic arteries simultaneously. This speed equals to the speed producing the normal average values in the model with the heart and the aorta. Numerical experiments show that for any artery the ratio between the average flow and the total outflow from the heart and the pump (if present) remains approximately the same in all considered cases without atherosclerosis.

In Section 3 we discuss the results, limitations, and open questions.

The following abbreviations are used in the present manuscript:

AA	Aortic arch
AV	Aortic valve
DCM	Dilated cardiomyopathy
HF	Heart failure
LA	Left atrium
LV	Left ventricle
LVAD	Left ventricular assist device
MV	Mitral valve
PV	Pulmonary veins
CA	Coronary artery
RAF	Relative average flow.

1. Materials and methods

1.1. The pump model

The scheme of LVAD installation is shown in Fig. 1. It connects the LV and the AA.

Dependency of the pressure drop across the LVAD and its periphery on the flow and the rotation speed is a mechanical characteristic of the pump which can be

measured in laboratory tests on a mock circulation setup. The pressure drop allows us to incorporate a pump model into a model of the cardiovascular system as a nonlinear lumped compartment. The pressure difference between the LV and the junction of the LVAD outlet and the aorta (point p in Fig. 1) is given by formula [6]

$$P_{lv} - P_p = aQ^2 + bQ\omega + c\omega^2 + d\frac{\mathrm{d}Q}{\mathrm{d}t} + P_{\mathrm{rec}} - P_{\mathrm{ext}} \tag{1.1}$$

where P_p is the pressure at point p, P_{lv} is the pressure in the LV, Q is the flow through the pump, ω is the rotation speed. Equation (1.1) includes characteristics of the external (periphery) part which connects the pump to the LV and the aorta

$$P_{\mathrm{rec}} = \begin{cases} 0, & Q > e\omega, \\ R_{\mathrm{rec}}\left(Q - e\omega\right)^2, & Q \leqslant e\omega, \end{cases} \qquad P_{\mathrm{ext}} = -L_{\mathrm{ext}}\frac{\mathrm{d}Q}{\mathrm{d}t} + R_{\mathrm{ext}}Q_p\left|Q_p\right|. \tag{1.2}$$

The physical meaning of the terms in (1.1) is as follows [6]. The theoretical Euler head equation gives the terms proportional to ω^2 and $Q\omega$. The fluid friction losses produce quadratic growth (Q^2) with the flow elevation. The flow detachment at the leading and trailing edges of the blade is responsible for eddy and separation losses proportional to ω^2, $Q\omega$, and Q^2. Part-load recirculation in the blade channels partly blocks them, decreases their effective diameter and increases the head pressure. This gives $\left(Q - e\omega\right)^2$ term. The flow inertia term is proportional to $\mathrm{d}Q/\mathrm{d}t$. Fluid friction and inertia frequency-dependent losses in the peripheral part of the LVAD are described by P_{ext} in (1.2). We refer to [6] and references therein for more details.

In our previous work [42] we used laboratory experiments with the paediatric mock circulation with Sputnik D [29,46,47] and the adult mock circulation for Sputnik 2 [29, 35] to validate (1.1). The mock circulation setups imitate physiological conditions in adults and paediatric patients. In particular, they include the Frank–Starling autoregulation mechanism which controls the cardiac output depending on the ventricle preload.

The parameters of model (1.1) for Sputnik D and Sputnik 2 were identified by the damped least-squares method (Levenberg–Marquardt algorithm) [20, 24]. We smoothed up the raw data by Savitzky-Golay filter [32] for computing time derivatives of the flow and the rotational speed of the pump. The coefficient of determination R^2 was used as the best-fit criterion. The parameters of model (1.1) for HeartMate II are taken from [6]. The parameters of Sputnik D, Sputnik 2, and HeartMate II as well as the coefficient of determination for Sputnik D and Sputnik 2 are shown in Table 1.

In the following sections we incorporate the LVAD model (1.1) into a lumped model of the heart coupled with a 1D network model of the blood flow in the systemic arteries and study the impact of the pump rotation speed on the systemic circulation in cases of installation of Sputnik D, Sputnik 2, and HeartMate II.

Table 1. Parameters and coefficients of determination (R^2) of the model (1.1).

Parameter	Unit	Sputnik D [42]	Sputnik 2 [42]	HeartMate II [6]
a	mm Hg/(L/min)^2	0.48	-0.46	-0.86
b	mm Hg/(rpm·L/min)	$-1.52\cdot10^{-3}$	$-5.64\cdot10^{-4}$	$3.21\cdot10^{-4}$
c	mm Hg/rpm^2	$1.74\cdot10^{-6}$	$1.73\cdot10^{-6}$	$9.54\cdot10^{-7}$
d	mm Hg·s^2/L	-60.06	-85.91	-22.97
e	(L/min)/rpm	$4.92\cdot10^{-5}$	$-3.70\cdot10^{-4}$	$3.59\cdot10^{-4}$
R_{rec}	mm Hg/(L/min)^2	5.63	5.59	3.07
L_{ext}	mm Hg·s^2/L	19.33	19.33	20
R_{ext}	mm Hg/(L/min)^2	0.35	0.35	0.38
R^2	—	0.96	0.97	—

1.2. 1D network haemodynamic model

The blood flow in large systemic arteries is described by a 1D reduced order model of unsteady flow of viscous incompressible fluid in a network of elastic tubes. Figure 2 represents the network of accounted systemic arteries which does not include the coronary arteries. The structure of the cerebral part of the network is based on [2, 8, 40]. The structure of the other systemic arteries is taken from [7]. The aorta is connected to the LV at the inlet and to the LVAD compartment between the segments 1b and 1c (see Fig. 2) similarly to [42]. The network of the coronary arteries [14] is shown in Fig. 3. The coronary arteries start from the junction between the segments 1a and 1b of the aorta (see Figs. 2, 3). We assume that the pump is connected to the aorta at the AA before the carotid arteries. The terminal arteries are connected to the corresponding Windkessel compartments at their outlets.

For reviews and details of 1D haemodynamic models we refer to [5, 39, 50, 51]. Algorithms of patient-specific parameter identification in such models were suggested in [10, 12, 15, 16]. Here, we briefly present this approach. Equations describing the flow in a vessel are based on mass and momentum conservation

$$\frac{\partial \mathbf{V}}{\partial t}+\frac{\partial \mathbf{F}(\mathbf{V})}{\partial x}=\mathbf{G}(\mathbf{V}) \tag{1.3}$$

$$\mathbf{V}=\begin{pmatrix} A \\ u \end{pmatrix}, \quad \mathbf{F}(\mathbf{V})=\begin{pmatrix} Au \\ u^2/2+p(A)/\rho \end{pmatrix}, \quad \mathbf{G}(\mathbf{V})=\begin{pmatrix} 0 \\ \psi \end{pmatrix}$$

where t is the time, x is the distance along the vessel counted from the vessel junction point, $\rho=1.04\,\text{g/cm}^3$ is the blood density, $A(t,x)$ is the vessel cross-section area, p is the blood pressure, $u(t,x)$ is the linear velocity averaged over the cross-section, ψ is the friction force

$$\psi=-8\pi\mu\frac{u}{\rho A} \tag{1.4}$$

and $\mu=4\,cP$ is the dynamic viscosity of the blood. The elasticity of the vessel wall material is characterized by the $p(A)$ relationship

$$p(A)=\rho_w c_0^2 f(A) \tag{1.5}$$

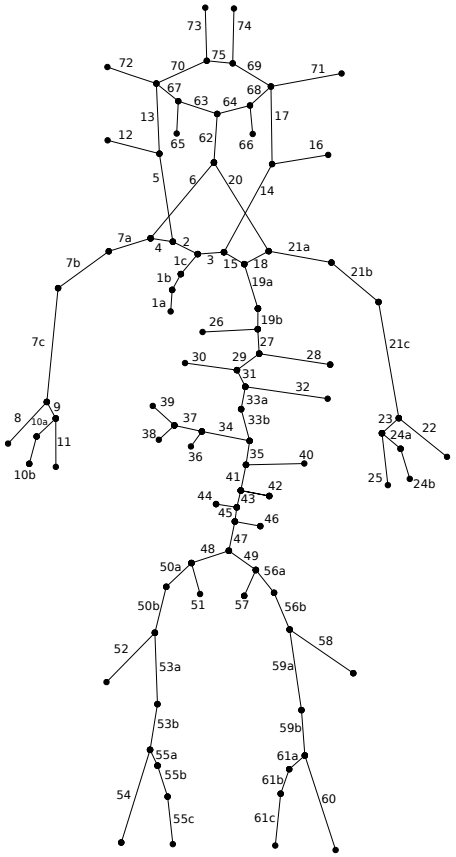

Figure 2. Scheme of the systemic arteries.

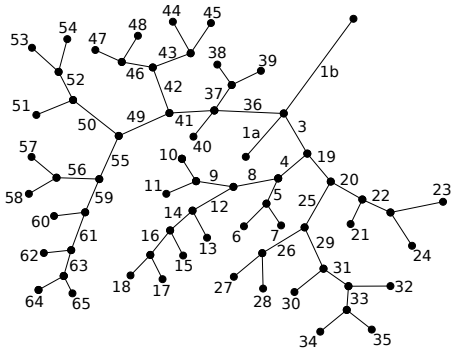

Figure 3. Scheme of the coronary arteries.

where ρ_w is the density of the vessel wall material, c_0 is the velocity of small disturbances propagation in the vessel wall, $f(A)$ is a monotone S-like function (see [52] for the review of the other options):

$$f(A) = \begin{cases} \exp(\eta - 1) - 1, & \eta > 1, \\ \ln \eta, & \eta \leqslant 1, \end{cases} \qquad \eta = \frac{A}{A_0} \tag{1.6}$$

where A_0 is the cross-sectional area of the unstressed vessel.

A model of autoregulation is applied to the systemic arteries except for the coronary part. It changes the elasticity of each vessel (coefficient c_0 in (1.5)) depending on the change of average pressure [16, 39, 51, 53]. The haemodynamic model of the coronary circulation accounts for myocardium contraction via a threefold increase of the peripheral resistance during systole [14, 16].

The mass conservation condition at the aortic root includes the blood flow through the AV Q_{ao}, which is also a variable of the heart model from Section 1.3:

$$u_{1a}(t,0) A_{1a}(t,0) = Q_{ao}(t)\,. \tag{1.7}$$

Boundary conditions at the connection of the aorta and the pump include the mass conservation condition

$$u_{1b}(t,L_{1b})A_{1b}(t,L_{1b}) + Q_{\text{pump}} = u_{1c}(t,0)A_{1c}(t,0) \tag{1.8}$$

and the total pressure continuity

$$p_{1b}(A_{1b}(t,L_{1b})) + \frac{\rho u_{1b}^2(t,L_{1b})}{2} = p_{1c}(A_{1c}(t,0)) + \frac{\rho u_{1c}^2(t,0)}{2} = p_p + \frac{\rho}{2}\left(\frac{Q_p}{A_p}\right)^2 \tag{1.9}$$

where p_p is the static pressure at the pump output, Q_p is the flow through the pump contributing to (1.1), A_p is the cross-section area of the tube which connects the output of the pump and the aorta.

Boundary conditions at the junctions of vessels include the mass conservation condition and the total pressure continuity

$$\sum_{k=k_1,k_2,\ldots,k_M} \varepsilon_k A_k(t,\tilde{x}_k)\, u_k(t,\tilde{x}_k) = 0 \tag{1.10}$$

$$p_k(A_k(t,\tilde{x}_k)) + \frac{\rho u_k^2(t,\tilde{x}_k)}{2} = p_{k+1}(A_{k+1}(t,\tilde{x}_{k+1})) + \frac{\rho u_{k+1}^2(t,\tilde{x}_{k+1})}{2} \tag{1.11}$$

where $k = k_1, k_2, \ldots, k_{M_j-1}$ is the index of the vessel, M_j is the number of the connected vessels at junction j, $\{k_1, \ldots, k_{M_j}\}$ is the range of the indices of the connected vessels at junction j, $\varepsilon = 1, \tilde{x}_k = L_k$ for incoming vessels, $\varepsilon = -1, \tilde{x}_k = 0$ for outgoing vessels.

The outflow boundary conditions assume that the terminal arteries are connected to the Windkessel compartments which describe the rest of the systemic circulation

$$\frac{\mathrm{d}Q_k}{\mathrm{d}t} = \frac{1}{R_{1,k}}\left(\frac{\mathrm{d}p_k(A_k(t,L_k))}{\mathrm{d}t} - \frac{\mathrm{d}P_{WK,k}}{\mathrm{d}t}\right) \tag{1.12}$$

$$\frac{\mathrm{d}P_{WK,k}}{\mathrm{d}t} = \frac{Q_k}{C_k}\left(1 + \frac{R_{1,k}}{R_{2,k}}\right) - \frac{p_k(A_k(t,L_k)) - p_\infty}{R_{2,k}C_k} \tag{1.13}$$

$$Q_k = u_k(t,L_k)A_k(t,L_k) \tag{1.14}$$

where $k = k_1, k_2, \ldots, k_N$ is the index of the vessel, N is the number of the terminal vessels, $\{k_1, \ldots, k_N\}$ is the range of the indices of the terminal vessels, $R_{1,k}, R_{2,k}, C_k$ are parameters presented in Table A3, $P_\infty = 7$ mm Hg for all compartments, $P_{WK,k}$ is the pressure in the Windkessel compartment.

The outflow boundary conditions for the terminal coronary vessels are different from those for the other terminal systemic arteries since they should account for myocardium contractions. We assume that a terminal coronary artery with index

k is connected to a compartment with the constant pressure p_∞ by the Poiseuille pressure drop condition

$$p_k\left(A_k\left(t,L_k\right)\right)-p_\infty=R_kA_k\left(t,L_k\right)u_k\left(t,L_k\right) \tag{1.15}$$

with the hydraulic resistance R_k which is increased by 200% during systole [14].

The boundary conditions at the aortic root (1.7), at the connection of the aorta and the pump (1.8), (1.9), at the vessel junctions (1.10), (1.11), at the terminal points of the systemic arteries (1.12)–(1.14), and at the terminal points of the coronary arteries (1.15) include a compatibility condition for the hyperbolic system (1.3) [5, 16,51]. Time discretization of (1.12), (1.13) by the implicit backward Euler method and the other systems of nonlinear algebraic equations are solved numerically by the Newton method. The hyperbolic system (1.3) inside every segment is solved numerically by the second order grid-characteristic method [5,23,51].

Parameters of the 1D network haemodynamic model in systemic arteries are given in Tables A1, A2. Parameters of the cerebral arteries are taken from [40]. The lengths and diameters of the other systemic arteries were borrowed from [7]. Parameters of the Windkessel compartments [7] are given in Table A3. The Windkessel resistances are multiplied by a constant to recover the well known systolic and diastolic aortic pressures in the normal conditions.

1.3. Lumped model of the heart with valve dynamics

The two chamber model of the left heart comprises the LV and the left atrium (LA), the MV and AV. It connects the pulmonary veins (PV) with the aorta whereas the LVAD compartment connects the LV with the aorta (see Fig. 1). The lumped model of the heart relates the dynamics of the volume and pressure of the heart chambers, the flow through the chambers, the pressure losses across the valves and PV–LA connection and dynamics of the valve opening.

The dynamics of the volume and pressure of the heart chambers may be described by lumped compartment model using variable elasticity concept [43, 54] and accounting for viscoelasticity of the myocardium [21,38,45]:

$$I_k\frac{\mathrm{d}^2V_k}{\mathrm{d}t^2}+R_kP_k\frac{\mathrm{d}V_k}{\mathrm{d}t}+E_k\left(t\right)\left(V_k-V_k^0\right)+P_k^0=P_k \tag{1.16}$$

where indices $k\in\{lv,la\}$ refer to the LV and the LA, respectively, $V_k(t)$ is the volume of the chamber k, $P_k(t)$ is the pressure in the chamber, V_k^0 and P_k^0 are the reference volume and pressure in the chamber, I_k is the inertia coefficient of the chamber, R_k is the hydraulic resistance coefficient of the chamber. The viscoelastic term is proportional to $P_k\,\mathrm{d}V/\mathrm{d}t$. Similar to [18,19,21,41] we set variable elasticity of the chambers $E_k(t)$ by

$$E_k\left(t\right)=E_{k,d}+\frac{1}{2}\left(E_{k,s}-E_{k,d}\right)e_k\left(t\right) \tag{1.17}$$

where $E_{k,d}$ and $E_{k,s}$ are end diastolic and end systolic elasticity constants (rf. Table 2), $0 \leqslant e_k(t) \leqslant 2$. For the LV we set

$$e_{lv}(t) = \begin{cases} 1 - \cos\left(\dfrac{t}{T_{s1}}\pi\right), & 0 \leqslant t \leqslant T_{s1} \\ 1 + \cos\left(\dfrac{t - T_{s1}}{T_{s2} - T_{s1}}\pi\right), & T_{s1} < t < T_{s2} \\ 0, & T_{s2} \leqslant t \leqslant T \end{cases} \tag{1.18}$$

for the LA we set

$$e_{la}(t) = \begin{cases} 0, & 0 \leqslant t \leqslant T_{pb} \\ 1 - \cos\left(\dfrac{t - T_{pb}}{T_{pw}}2\pi\right), & T_{pb} < t < T. \end{cases} \tag{1.19}$$

The values of parameters T_{s1}, T_{s2}, T_{pb}, T_{pw} are presented in Table 2.

The mass conservation law for the LV and the LA relates the flow through the heart chambers and the change of their volume

$$\begin{aligned} \frac{\mathrm{d}V_{lv}}{\mathrm{d}t} &= Q_{mi} - Q_{ao} - Q_p \\ \frac{\mathrm{d}V_{la}}{\mathrm{d}t} &= Q_{pv} - Q_{mi} \end{aligned} \tag{1.20}$$

where Q_{mi} is the flow through the MV, Q_{ao} is the flow through the AV, Q_p is the flow through the LVAD, Q_{pv} is the flow from the PV. The model of heart dynamics is combined with the 1D arterial haemodynamic model by Q_{ao} in (1.7).

For unsteady flow in a channel with a variable cross-section, the pressure drop satisfies the relation [21, 56]:

$$\Delta P = L(g)\frac{\mathrm{d}Q}{\mathrm{d}t} + \alpha(g)Q + \beta(g)Q|Q|. \tag{1.21}$$

We set the pressure drop $\Delta P = P_{pv} - P_{la}$ for the PV–LA connection, $\Delta P = P_{la} - P_{lv}$ for the LA–LV connection, and $\Delta P = P_{lv} - p(A_{1a}(t,0))$ for the LV–AA connection. Here $g(\vartheta) = \left\{\vartheta^{\min} \leqslant \vartheta \leqslant \vartheta^{\max}, 0 \leqslant g(\vartheta) \leqslant 1\right\}$ is a smooth monotone function of the angle of the MV and the AV opening ϑ for $k \in \{mi, ao\}$ [18]:

$$g(\vartheta_k) = \begin{cases} \dfrac{\left(1 - \cos\vartheta_k^{\min}\right)^2}{\left(1 - \cos\vartheta_k^{\max}\right)^2}, & \vartheta_k < \vartheta_k^{\min} \\ \dfrac{\left(1 - \cos\vartheta_k\right)^2}{\left(1 - \cos\vartheta_k^{\max}\right)^2}, & \vartheta_k^{\min} \leqslant \vartheta_k \leqslant \vartheta_k^{\max} \\ 1, & \vartheta_k > \vartheta_k^{\max}. \end{cases} \tag{1.22}$$

The value $g(\vartheta^{\min})$ corresponds to the completely closed state of the valve, while the value $g(\vartheta^{\max}) = 1$ corresponds to the completely opened state of the valve. For $L = 0$, $\beta = 0$, $\alpha \neq 0$ equation (1.21) transforms to the Poiseuille pressure drop condition which accounts for the viscous friction losses. By analogy with [27,44] we neglect this term and set $\alpha = 0$ for all cases. For $L = 0$, $\alpha = 0$, $\beta \neq 0$ equation (1.21) transforms to the orifice pressure drop condition. The first term in (1.21) accounts for the inertia of non-stationary flow. The coefficient β is defined by [34, 55, 56]:

$$\beta(A_k) = \frac{\rho}{2B_k}\left(\frac{1}{\tilde{A}_k} - \frac{1}{A_k}\right)^2, \quad k \in \{mi, ao\} \tag{1.23}$$

where parameters $\tilde{A}_{mi}$, B_{ao}, and B_{mi} are given in Table 2, $\tilde{A}_{ao} = A_{1a}(t,0)$. For the PV–LA connection $\beta = \text{const}$. For both MV and AV, their cross-section A_k depends on the angle of the valve opening, $A_k(\vartheta_k) = A_k^{\max} g(\vartheta_k)$.

Dynamics of the MV and the AV is governed by the second Newton law. The pressure gradient across the valve, vorticity generation and shear forces acting on the valve leaflets [36] have to be accounted by the model [18, 19]. In this work we set the valve dynamics equations as

$$\frac{\mathrm{d}^2\vartheta_k}{\mathrm{d}t^2} = -K_k^f \frac{\mathrm{d}\vartheta_k}{\mathrm{d}t} + \Delta P_k K_k^p \cos\vartheta_k - F_k^r(\vartheta_k), \quad k \in \{mi, ao\} \tag{1.24}$$

where $\vartheta_{ao}(t)$ is the angle of the AV opening, $\vartheta_{mi}(t)$ is the angle of the MV opening, K_k^f and K_k^p are the parameters presented in Table 2, $\Delta P_{ao} = P_{lv} - P_{ao}$, $\Delta P_{mi} = P_{la} - P_{lv}$, the first term at the right-hand side corresponds to the friction force, the second term corresponds to the pressure force driving the valve motion, F^r is the force which helps to avoid physiologically abnormal valve positions ($\vartheta_k < \vartheta_k^{\min}$ and $\vartheta_k > \vartheta_k^{\max}$)

$$F^r(\vartheta) = \begin{cases} 0, & \vartheta^{\min} \leqslant \vartheta \leqslant \vartheta^{\max} \\ e^{10^3(\vartheta - \vartheta^{\max})} - 1, & \vartheta > \vartheta^{\max} \\ 1 - e^{10^3(\vartheta^{\min} - \vartheta)}, & \vartheta < \vartheta^{\min}. \end{cases} \tag{1.25}$$

The other forces are neglected. All parameters of the lumped model of the left heart are collected in Table 2.

1.4. Haemodynamic model of the systemic circulation

Parameters of the integrated model including the 1D network model of the systemic circulation and the lumped model of the heart with valve dynamics for healthy conditions are collected in Tables 2, A1. Simulations with these parameters without LVAD produce the values of the LV stroke volume, systolic and diastolic pressures in the aortic root which are in a good agreement with the well-known physiological data [4, 33] and with our previous simulations with a reduced 1D haemodynamic model of the aorta represented by two segments instead of multiple systemic arteries [42].

Table 2. Parameters of the lumped model of the left heart [42].

Parameter	Unit	Value	Reference	Parameter	Unit	Value	Reference
$E_{lv,s}$	mm Hg/ml	4.0	[42]	$\vartheta_{ao}^{\min}$		0°	[41]
$E_{lv,d}$	mm Hg/ml	0.09	[42]	$\vartheta_{ao}^{\max}$		75°	[18]
I_{lv}	mm Hg· s^2/ml	10^{-7}	[42]	$\vartheta_{mi}^{\min}$		0°	[41]
R_{lv}	s/ml	$1.5\cdot10^{-3}$	[38]	$\vartheta_{mi}^{\max}$		75°	[18]
$E_{la,s}$	mm Hg/ml	1.2	[42]	V_{lv}^{0}	ml	5	[42]
$E_{la,d}$	mm Hg/ml	0.3	[42]	V_{la}^{0}	ml	4	[42]
I_{la}	mm Hg· s^2/ml	10^{-7}	[42]	T_{s1}	s	0.3	[18]
R_{la}	s/ml	$1.5\cdot10^{-3}$	[38]	T_{s2}	s	0.35	[18]
T_{pw}	s	0.1	[18]	T_{pb}	s	0.9	[18]
K^p	rad/s^2· mm Hg	10^4	[42]	K^f	rad/s	50	[18]
P_{pv}	mm Hg	13	[42]	S_p	cm^2	1.1	[42]
L_{pv}	mm Hg· s^2/ml	10^{-2}	[42]	β_{pv}	mm Hg· s^2/ml^2	$4\cdot10^{-4}$	[42]
L_{mi}	mm Hg· s^2/ml	$5\cdot10^{-10}$	[42]	B_{mi}		300	[42]
L_{ao}	mm Hg· s^2/ml	$5\cdot10^{-5}$	[42]	B_{ao}		500	[42]
$\tilde{A}_{mi}$	cm^2	5	[42]	$A_{ao}^{\max}$	cm^2	4	[42]
T	s	1	[42]	$A_{mi}^{\max}$	cm^2	4	[42]

The present 1D network model of the systemic circulation consists of several parts including coronary, cerebral and other systemic arteries. All these parts have been validated in the appropriate works [2,7,8,14,40]. Parameters of major systemic arteries were taken from ADAN56 model [7]. Cerebral arteries, including the circle of Willis, and arteries of the neck were extracted from CT scans of an anonymous patient [13]. Data from [2] complete the circle of Willis and allow us to impose boundary conditions at the outlets of cerebral arteries.

The structure of coronary arteries is extracted from a generalized anatomically correct 3D model [14]. Parameters c_0 from (1.5) were adjusted according to the pulse wave velocity estimations in left and right coronary arteries (CA) [1]. Resistances of the outlets of terminal CAs are divided in proportion to the diameters of the major CAs according to the Murray's law with the power 2.27 [14]. The total hydraulic resistances of the CAs are set according to the assumption that the coronary blood flow consumes 5% of the total cardiac output in the normal conditions.

2. Results

2.1. Haemodynamic simulations in systemic arteries for HF associated with LV DCM and supported by LVAD

We compute haemodynamic characteristics of the left heart and major systemic arteries under HF conditions in the presence of the examined LVAD (Sputnik 2, Sputnik D, and HeartMate II) operating at various rotation speeds. In this work we consider late stages of HF accompanied with LV DCM. The latter is the common indication for the long term LVAD installation. LV DCM is characterized by decreased LV contractility, thinning of the LV wall and increased cavity volume of the LV. These changes produce substantial decrease in the LV pressure, substantial elev-

Table 3. Modified parameters of the LV DCM heart model [42].

Parameter	Unit	Value	Parameter	Unit	Value
P_{pv}	mm Hg	10	$V_{0,lv}$	ml	20
$E_{lv,d}$	mm Hg/ml	0.04	R_{lv}	s/ml	$5 \cdot 10^{-4}$
$E_{lv,s}$	mm Hg/ml	0.44	R_{la}	s/ml	$5 \cdot 10^{-4}$
$E_{la,s}$	mm Hg/ml	1.1			

Table 4. Rotation speed of the pump (rpm) for the important cardiovascular conditions.

Conditions	Sputnik 2	Sputnik D	HeartMate II
Zero flow through the pump achieved	$5.75 \cdot 10^3$	$8.5 \cdot 10^3$	$7 \cdot 10^3$
Permanent closure of the AV	$7 \cdot 10^3$	$12 \cdot 10^3$	$8 \cdot 10^3$
Permanent opening of the MV	$11.5 \cdot 10^3$	—	$13.5 \cdot 10^3$
Normal value of the total ejected volume achieved	$8.5 \cdot 10^3$	$15 \cdot 10^3$	10^4
Normal average values of the velocity, pressure and flow in the distal arteries achieved	$8.5 \cdot 10^3$	$15 \cdot 10^3$	10^4

ation of the LV volume, late opening of the AV, substantial reduction of the cardiac output and related cardiovascular dysfunctions. LVAD unloads the LV and decreases its volume by redirecting a portion of blood to the aorta through the pump.

In order to simulate LV DCM conditions, we modify some parameters of the heart model as shown in Table 3. The other parameters from Table 2 remain intact. We note that myocardium contractions for patients with LV DCM may be different from those for healthy subjects. Thus the hydraulic resistance coefficient R_k in (1.15) should be modified. However, the compressing force was not clinically determined to correlate with the decrease of the coronary flow reserve in the left anterior descending artery (vessels 4, 8, 12, 14 in Fig. 3) in patients with non-ischemic DCM [31]. Thus we set R_k to values typical for healthy subjects [14].

The simulations with these parameters produce results which correlate with published data [9, 25, 42].

We analyze the impact of the three pumps by setting the same parameters of the heart function and systemic arteries for all pumps. The recommended operating conditions of the pump are defined as follows [42, 49]:

1. The AV should be opened at least for a short period during the cardiac cycle;
2. The flow through the pump should be directed from the LV to the aorta;
3. The ventricular suction is not admitted;
4. The total ejected volume per cardiac cycle in the aorta should be equal to the physiological value in the normal conditions.

We study haemodynamic characteristics of the left heart and systemic arteries for a wide range of the rotation speed of the pumps. We note that the technical and clinical restrictions confine the range of the rotation speed. For Sputnik 2 the range is $5 \cdot 10^3$–10^4 rpm, for Sputnik D the range is $6 \cdot 10^3$–$2 \cdot 10^4$ rpm, for HeartMate II the range is $6 \cdot 10^3$–$15 \cdot 10^3$ rpm. Results of the simulations are summarized in Table 4.

Positive flow through the pump without permanent closure of the AV is achieved in the range $5.75 \cdot 10^3$–$7 \cdot 10^3$ rpm for Sputnik 2, $8.5 \cdot 10^3$–$12 \cdot 10^3$ rpm for Sputnik D and $7 \cdot 10^3$–$8 \cdot 10^3$ rpm for HeartMate II. The total ejected volume from the pump and LV equals to the normal physiological value at $8.5 \cdot 10^3$ rpm for Sputnik 2, $15 \cdot 10^3$ rpm for Sputnik D and 10^4 rpm for HeartMate II. The extremal condition of the permanent opening of the MV is associated with zero work of the LV [42] and is achieved beyond the normal operating conditions. All the above conditions are achieved at the same value of rotation speed as these results match the rotation speeds computed by the lumped model of the heart with valve dynamics, LVAD and the reduced 1D haemodynamic model in the aorta represented by two segments [42].

Recovery of the average values of the flow, pressure and linear velocity to the normal values occurs at $8.5 \cdot 10^3$ rpm for Sputnik 2, $15 \cdot 10^3$ rpm for Sputnik D, and 10^4 rpm for HeartMate II (the last row in Table 4) in all arteries of the 1D network presented in Figs. 2 and 3. We show dependencies of average flow and average pressure on the rotation speed for the left coronary artery 3 (Fig. 4), for the right anterior cerebral artery 70 (Fig. 5), for the left common carotid artery 14 (Fig. 6), for the distal part of the abdominal aorta 47 (Fig. 7), and for the left anterior tibial artery 60 (Fig. 8). The indices and positions of the vessels correspond to Tables A1, A2 and Figs. 2, 3, respectively. The horizontal solid line in Figs. 4–8 represents the average value in healthy subjects (without HF and LVAD). The dependencies in the other vessels are similar. The linear velocity is calculated from known pressure and flow, and the dependencies of the average linear velocity on the rotation speed are similar.

From Table 4 we notice that recovery of the total ejected volume and the average flow, pressure and linear velocity to normal values occurs at the same value of the rotation speed for each pump (the optimal rotation speed corresponds to the intersection of the flow or pressure curves with the horizontal solid line in Figs. 4–8). Therefore, the recovery of the total ejected volume is the sufficient condition for the recovery of the average haemodynamic characteristics of the systemic circulation without atherosclerosis.

In Figs. 9 and 10, we compare the impact of the LVADs operating at the optimal rotation speed on the LV volume and the parameters of the heart outflow. The left part of Fig. 9 shows variations of the LV volume in time. We observe that the LV volume is approximately equal to the average between the LV volume in the normal and HF conditions. The right part of Figs. 9 and 10 show variations of the aortic flow, linear velocity and pressure in time. In the absence of LVAD we consider the flow through the AV. In the presence of LVAD we consider the total (cumulative) flow from the heart and the pump (i.e., the input flow to the vessel 1c in Fig. 2). The velocity and the pressure are considered in the middle of the vessel 1c. We observe that all pumps produce the values of flow, velocity and pressure which are very close to the corresponding average values in the normal conditions.

To study the influence of flow regimes on blood distribution in systemic arteries, we evaluate the ratio of the average flow (RAF) in the middle point of every vessel to the average flow through the AV in the cases without LVAD and to the average

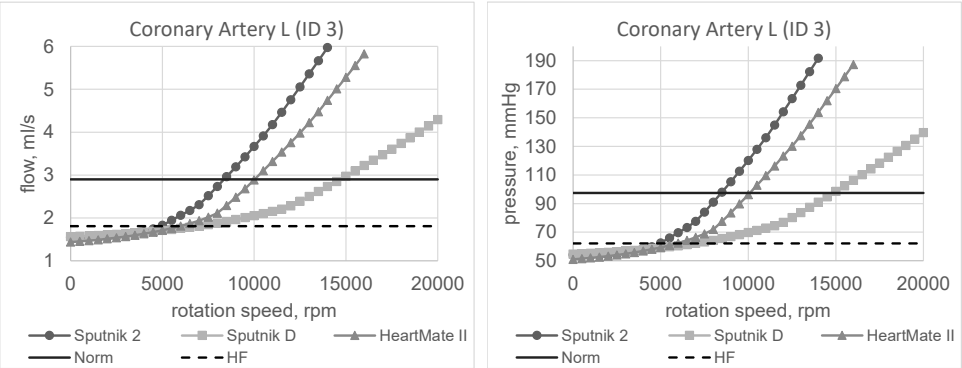

Figure 4. Average flow (left) and pressure (right) in the left coronary artery in normal and HF (heart failure) conditions, and in HF supported by LVAD Sputnik 2, Sputnik D, and HeartMate II.

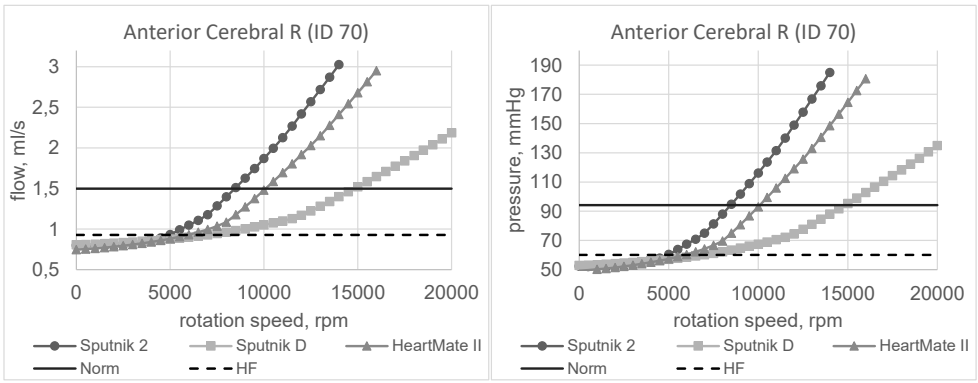

Figure 5. Average flow (left) and pressure (right) in the right anterior cerebral artery in normal and HF (heart failure) conditions, and in HF supported by LVAD Sputnik 2, Sputnik D, and HeartMate II.

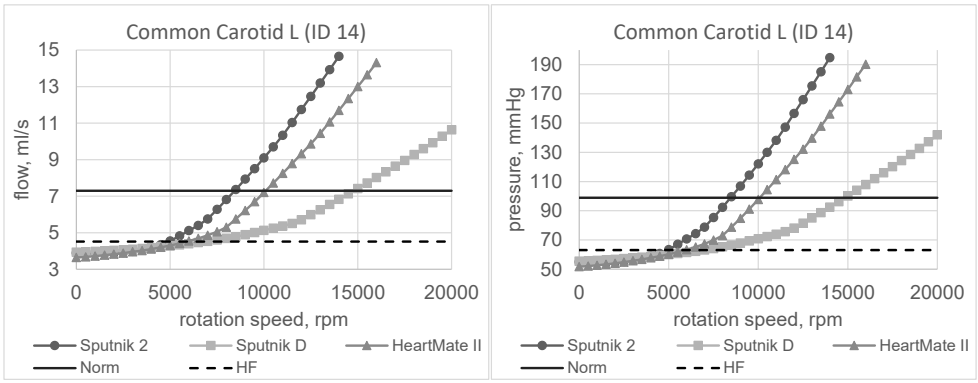

Figure 6. Average flow (left) and pressure (right) in the left common carotid artery in normal and HF (heart failure) conditions, and in HF supported by LVAD Sputnik 2, Sputnik D, and HeartMate II.

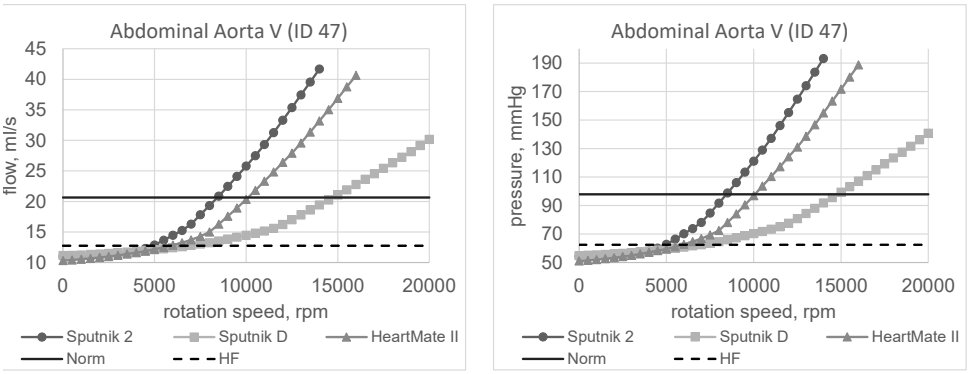

Figure 7. Average flow (left) and pressure (right) in the abdominal aorta in normal and HF (heart failure) conditions, and in HF supported by LVAD Sputnik 2, Sputnik D, and HeartMate II.

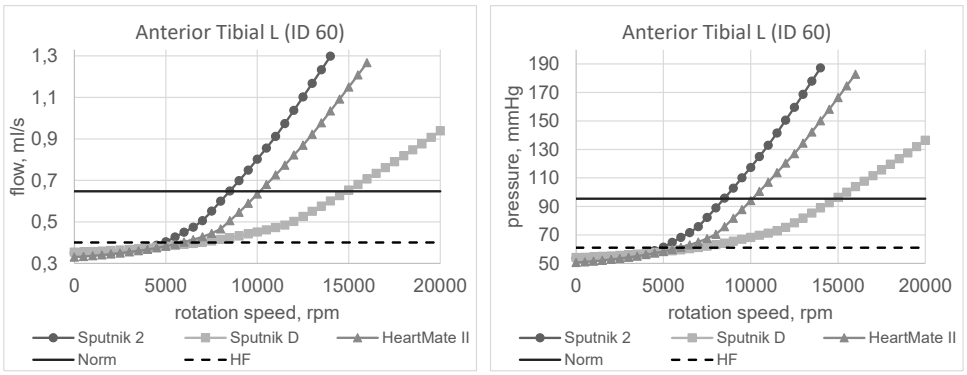

Figure 8. Average flow (left) and pressure (right) in the left anterior tibial artery in normal and HF (heart failure) conditions, and in HF supported by LVAD Sputnik 2, Sputnik D, and HeartMate II.

flow through the vessel 1c in the cases with LVAD. In Tables A1, A2 we present in every vessel the mean RAF (averaged RAFs) for the healthy case, the HF case and HF supported by Sputnik 2 cases at the rotation speeds $4 \cdot 10^3 + j \cdot 10^3$ rpm, $j = 0, \ldots, 8$. The relative standard deviation for these RAFs is less than 1% for all vessels except the anterior communicating artery (3%). The relative difference between the maximum and minimum RAFs to the mean RAF in every vessel is less than 2.5% except the anterior communicating artery (12%) and two first segments of the ascending aorta. The segments of the ascending aorta are excluded from the analysis as the pumps strongly affect the blood flow there. Therefore, in most arteries RAF remains the same in all considered conditions. The other pumps (Sputnik D, HeartMate II) produce similar results in the corresponding ranges of the rotation speed. Thus, within our model the blood distribution in the systemic vessels does not depend on flow regime in the aorta.

In summary, all considered LVADs produce approximately the same impact both on the haemodynamic characteristics in distal vessels and in the heart. All pumps are capable of recovering the average normal values at the optimal rotation speeds

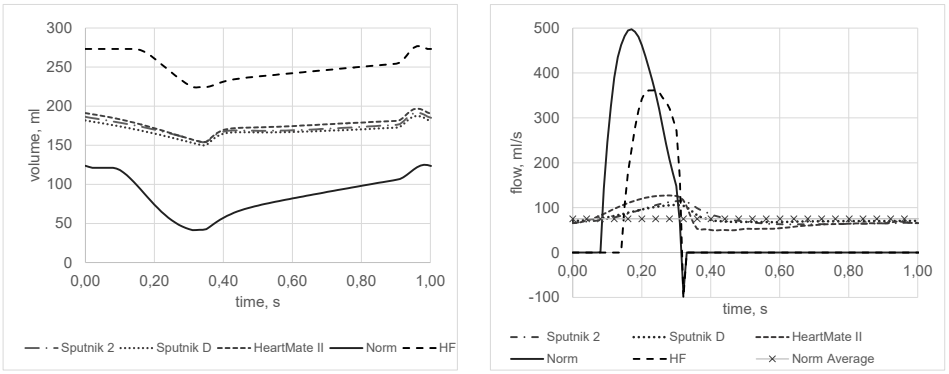

Figure 9. The LV volume (left) and the total aortic flow (right) in the normal and HF (heart failure) conditions, and in HF supported by LVAD at $8.5 \cdot 10^3$ rpm for Sputnik 2, $15 \cdot 10^3$ rpm for Sputnik D, and 10^4 rpm for HeartMate II.

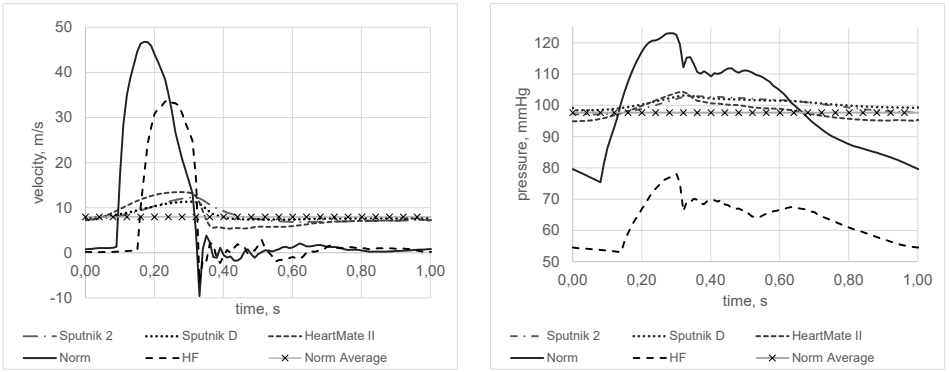

Figure 10. The velocity (left) and the pressure (right) in the aorta **1c** (rf. Fig. 2) in the normal and HF (heart failure) conditions, and in HF supported by LVAD at $8.5 \cdot 10^3$ rpm for Sputnik 2, $15 \cdot 10^3$ rpm for Sputnik D, and 10^4 rpm for HeartMate II.

which are different for every pump. The optimal rotation speeds produce positive flows through the pump and permanent closure of the AV. The latter phenomenon should be addressed in future clinical studies.

2.2. Computational analysis of LVAD supported systemic circulation in the presence of atherosclerosis

Various pathological conditions affect significantly the arterial blood flow. Our model allows us to analyze the impact of LVAD on circulation in patients with LV DCM and atherosclerosis. An atherosclerotic plaque is imitated by inserting a narrow vascular segment with 90% decrease of the diameter [11]. We imitated atherosclerosis in the leg (the left femoral artery 59a in Fig. 2), in the heart (the left anterior descending artery 4 in Fig. 3), and in the neck (the right and left common carotid arteries 5 and 14 in Fig. 2).

Table 5. The optimal rotation speeds (rpm) which recover average blood flows in atherosclerotic networks to the values with the heart without LV DCM and LVAD.

Vessels	Sputnik 2	Sputnik D	HeartMate II
Coronary arteries (4, 5, 8, 12, 17, 19, 33, 41, in Fig. 3)	$8.5 \cdot 10^3$	$14.8 \cdot 10^3$	$10.25 \cdot 10^3$
Cerebral arteries (14, 17, 62, 68, 70, 75, in Fig. 2)	$8.58 \cdot 10^3$	$15 \cdot 10^3$	$10.3 \cdot 10^3$
Arteries of the leg (48, 56b, 59a, 61c, in Fig. 2)	$8.6 \cdot 10^3$	$14.95 \cdot 10^3$	$10.3 \cdot 10^3$

Table 6. The relative (%) flow rate (compared to the healthy vasculature and heart) in different arteries of atherosclerotic regions, at increased rotation speeds.

ID	Vessel title	Sputnik 2	Sputnik D	HeartMate II
4	Left anterior descending I	14.61	10.25	9.91
5		14.61	10.26	9.91
8	Left anterior descending II	14.59	10.24	9.89
17		14.56	10.22	9.87
19	Left circumflex artery I	169.82	122.80	118.89
33		170.02	122.86	118.94
41	Right coronary artery I	170.02	122.82	118.90
14	Common carotid left	47.29	33.90	32.81
13	Internal carotid right	7.75	5.12	4.91
17	Internal carotid left	7.84	5.18	4.97
75	Anterior communicating artery	7.73	9.90	9.94
62	Basilar	989.30	721.46	699.37
68	Posterior communicating left	1247.76	911.49	883.71
70	Anterior cerebral Right I	110.69	79.96	77.45
48	Common iliac right	166.63	120.87	117.11
56b	Femoral left I	142.94	103.52	100.21
59a	Femoral left II	61.24	43.44	41.65
59b	Popliteal left I	61.15	42.78	41.68
61c	Posterior tibial left	61.12	42.54	41.69
	Rotation speed, rpm	$14 \cdot 10^3$	$20 \cdot 10^3$	$13 \cdot 10^3$
	Cumulative output, %	193.25	140.11	135.74

We studied the average blood flow characteristics in the distal, proximal and contralateral (with respect to the plaque) vessels in the coronary, cerebral, and leg regions and found the optimal rotation speeds of LVADs which recover the same average blood flows in the case of the heart without LV DCM and LVAD. The optimal rotation speeds are collected in Table 5.

The average blood flow recovers to a normal value at the same optimal rotation speed in all vessels of each vascular region. The optimal rotation speed depends on atherosclerotic vascular region. For instance, Sputnik 2 recovers the average blood flow in the coronary arteries at $8.5 \cdot 10^3$ rpm, in the cerebral arteries at $8.58 \cdot 10^3$ rpm and in the arteries of the leg at $8.6 \cdot 10^3$ rpm. The most sensitive to the rotation speed are flows in the proximal, contralateral and neighbouring arteries. The blood flow in the distal arteries is small and weakly depends on the pump speed. The presence of atherosclerosis in critical (coronary and cerebral) regions may change the optimal rotation speed up to 3%.

Further increase of the pump rotation speed may recover the blood flow in the arteries with atherosclerosis to normal values typical for healthy arteries, at the cost of increase of flow rates in healthy arteries. We checked this hypothesis by numerical simulations. In Table 6 we compare the average blood flow in the atherosclerotic network under the forced regime of LVAD supporting the heart with LV DCM and the same network without atherosclerosis and supplied by the heart without LV DCM. The cumulative output from the heart and the pump rises up to 135% – 193% of the normal value of the stroke volume of the heart (80 ml). The forced regimes of the pumps produce diverse relative flow rates (compared to the healthy vasculature and heart): $\sim$10% in the distal coronary and cerebral arteries, $\sim$50% in the distal leg arteries, whereas in the other arteries they may rise up to 1000% which is far beyond the safe regimes of the artery load.

3. Discussion

In this work we studied the impact of LVADs Sputnik 2, Sputnik D, and HeartMate II on haemodynamic characteristics of the left heart and the systemic circulation in a representative subject with HF associated with LV DCM. We took parameters of the heart and the LVAD models in the normal and LV DCM conditions from [42]. The 1D network model of the systemic circulation comprises the networks of coronary, cerebral and other systemic arteries described in [2, 7, 8, 14, 40].

Characteristics of the heart function and the aortic flow are very close to those of the reduced 1D model representing the aorta by two segments and single Windkessel compartment [42]. It means that the simplified model [42] is sufficient for analysis of the LVAD performance. In most arteries the fraction of the average blood flow to the aortic inflow from the heart and the pump (if present) remains approximately the same in all considered conditions for all the pumps.

We considered the recovery of the ejected blood volume, the average linear velocity, pressure and flow in distal arteries as the criterion of normal operating conditions of the pump. We note that in these conditions the pulse pressure is almost zero, the flow is non-pulsatile, and the AV is closed. Clinical studies are required to decide if this state is appropriate for patients.

In this work we observed that the normal average values of the velocity, pressure and flow as well as the normal values of the blood volume ejected by the LV and the pump, are achieved at the same rotation speed which we call the optimal rotation speed. The normal ejected volume and the normal average values of the linear velocity, pressure and flow are calculated in our model for a healthy subject without LVAD and coincide with the well-known physiological data. The normal pump operating conditions do not hold simultaneously for all considered LVADs, as the optimal rotation speed produces permanent closure of the AV.

We also observed that the normal average velocity, pressure and flow are achieved simultaneously at the same rotation speed for all vessels included in the 1D network. In general it is not the case: various pathologies (atherosclerosis, aneurysms, pathological tortuosity, increased stiffness of the vessels, incomplete Circle of Willis)

affect the recovery of the normal average characteristics and the optimal rotation speed may be sensitive to such pathologies. In particular, we observe that in the presence of atherosclerosis in the left anterior descending artery, in the common carotid arteries, or in the femoral artery, the flow recovery in the regions of coronary, cerebral and leg circulation is achieved at different pump rotation speeds.

References

1. J. Aguado-Sierra, K. H. Parker, J. E. Davies, D. Francis, A. D. Hughes, and J. Mayet, Arterial pulse wave velocity in coronary arteries. In: *Conf. Proc. IEEE Eng. Med. Biol. Soc.* (2006), 867–870.
2. J. Alastruey, K. H. Parker, J. Peiró, S. M. Byrd, and S. J. Sherwin, Modeling the circle of Willis to assess the effects of anatomical variations and occlusions on cerebral flows. *J. Biomech.* **40** (2007), No. 8, 1794–1805.
3. I. R. Argueta-Morales, R. Tran, A. Ceballos, W. Clark, E. Divo, A. J. Kassab, and W. M. DeCampli, Mathematical modeling of patient-specific ventricular assist device implantation to reduce particulate embolisation rate to cerebral vessels. *J. Biomech. Engrg.* **136** (2014), No. 7, 071008.
4. K. Barret, H. Brooks, S. Boitano, and S. Barman, *Ganong's Review of Medical Physiology, 23-rd edition*. The McGraw-Hill, 2010.
5. N. Bessonov, A. Sequeira, S. Simakov, Yu. Vassilevski, and V. Volpert, Methods of blood flow modelling. *Math. Modelling Natural Phenomena* **11** (2016), No. 1, 1–25.
6. S. Boës, B. Thamsen, M. Haas, M. S. Daners, M. Meboldt, and M. Granegger, Hydraulic characterisation of implantable rotary blood pumps. *IEEE Trans. Biomed. Engrg.* **66** (2018), No. 6, 1618–1627.
7. E. Boileau, P. Nithiarasu, P. J. Blanco, L. O. Müller, F. E. Fossan, L. R. Hellevik, W. P. Donders, W. Huberts, M. Willemet, and J. Alastruey, A benchmark study of numerical schemes for one-dimensional arterial blood flow modelling. *Int. J. Numer. Meth. Biomed. Engrg.* **31** (2015), No. 10, e02732.
8. D. V. Burenchev, F. Y. Kopylov, A. A. Bykova, T. M. Gamilov, D. G. Gognieva, S. S. Simakov, and Yu. V. Vasilevsky, Mathematical modelling of circulation in extracranial brachocephalic arteries at pre-operation stage in carotid endarterectomy. *Russ. J. Cardiology* **144** (2017), No. 4, 88–92.
9. L. G. E. Cox, S. Loerakker, M. C. M. Rutten, B. A. J. M. de Mol, and F. N. van de Vosse, A mathematical model to evaluate control strategies for mechanical circulatory support. *Artificial Organs* **33** (2009), No. 8, 593–603.
10. A. Danilov, Yu. Ivanov, R. Pryamonosov, and Yu. Vassilevski, Methods of graph network reconstruction in personalised medicine. *Int. J. Numer. Meth. Biomed. Engrg.* **32** (2016), No. 8, e02754.
11. N. El Khatib, O. Kafi, A. Sequeira, S. Simakov, Yu. Vassilevski, and V. Volpert, Mathematical modelling of atherosclerosis. *Math. Modelling Natur. Phenomena* **14** (2019), No. 6, 2019050.
12. T. Gamilov, Ph. Kopylov, and S. Simakov, Computational simulations of fractional flow reserve variability. *Lecture Notes in Comput. Sci. Engrg.* **112** (2016), 499–507.
13. T. Gamilov, S. Simakov, and Ph. Kopylov, Computational modeling of multiple stenoses in carotid and vertebral arteries. In: *Trends in Biomathematics: Modeling, Optimisation and Computational Problems* (Ed. R. Mondaini). Springer, Cham, 2018.
14. T. Gamilov, Ph. Kopylov, M. Serova, R. Syunayaev, A. Pikunov, S. Belova, F. Liang, J. Alastruey,

and S. Simakov, Computational analysis of coronary blood flow: the role of asynchronous pacing and arrhythmias. *Mathematics* **8** (2020), No. 8, 1205.

15. T. Gamilov, J. Alastruey, and S. Simakov, Linear optimisation algorithm for 1D haemodynamics parameter estimation. In: *Proc. of the 6th Europ. Conf. on Computational Mechanics: Solids, Structures and Coupled Problems, ECCM 2018 and 7th European Conference on Computational Fluid Dynamics, ECFD 2018* (Eds. R. Owen, R. de Borst, J. Reese, and C. Pearce). CIMNE, 2020, pp. 1845–1850.
16. T. Gamilov and S. Simakov, Blood flow under mechanical stimulations. *Advances in Intelligent Systems and Computing* **1028** (2020), No. AISC, 143–150.
17. G. A. Giridharan, T. J. Lee, M. Ising, et al, Miniaturization of mechanical circulatory support systems. *Artificial Organs*, **36** (2012), No. 8, 731–739.
18. T. Korakianitis and Y. Shi, Numerical simulation of cardiovascular dynamics with healthy and diseased heart valves. *J. Biomechanics* **39** (2006), No. 11, 1964–1982.
19. T. Korakianitis and Y. Shi, A concentrated parameter model for the human cardiovascular system including heart valve dynamics and atrioventricular interaction. *Medical Engrg. & Physics* **28** (2006), 631–628.
20. K. Levenberg, A method for the solution of certain nonlinear problems in least squares. *Quarterly of Applied Mathematics* **2** (1944), No. 2, 164–168.
21. F. Liang, S. Takagi, R. Himeno, and H. Liu, Multi-scale modeling of the human cardiovascular system with applications to aortic valvular and arterial stenoses. *Medical & Biological Engrg. & Computing* **47** (2009), 743–755.
22. K. M. Lim, I. S. Kim, S. W. Choi, B. G. Min, Y. S. Won, H. Y. Kim, and E. B. Shim, Computational analysis of the effect of the type of LVAD flow on coronary perfusion and ventricular afterload. *J. Physiol. Sci.* **59** (2009), 307–316.
23. K. M. Magomedov and A. S. Kholodov, *Grid-Characteristic Numerical Methods*. Urite, Moscow, 2018.
24. D. Marquardt, An algorithm for least-squares estimation of nonlinear parameters. *SIAM J. Appl. Math.* **11** (1963), No. 2, 431–441.
25. J. R. Martina, P. H. M. Bovendeerd, N. de Jonge, B. A. J. M. de Mol, J. R. Lahpor, and M. C. M. Rutten, Simulation of changes in myocardial tissue properties during left ventricular assistance with a rotary blood pump. *Artificial Organs* **37** (2013), No. 6, 531–540.
26. B. J. E. Misgeld, D. Rüschen, S. Schwandtner, S. Heinke, M. Walter, and S. Leonhardt, Robust decentralised control of a hydrodynamic human circulatory system simulator. *Biomedical Signal Processing and Control* **20** (2015), 35–44.
27. J. P. Mynard, M. R. Davidson, D. J. Penny, and J. J. Smolich, A simple, versatile valve model for use in lumped parameter and one-Dimensional cardiovascular models. *Int. J. Numer. Meth. Biomed. Engrg.* **28** (2012), No. 6-7, 626–641.
28. D. S. Petukhov and D. V. Telyshev, Control algorithms for rotary blood pumps used in assisted circulation. *Biomed. Engrg.* **50** (2016), No. 3, 157–160.
29. A. A. Pugovkin, A. Markov, S. V. Selishchev, L. Korn, M. Walter, SS. Leonhardt, L. A. Bockeria, O. L. Bockeria, and D. V. Telyshev, Advances in haemodynamic analysis in cardiovascular diseases investigation of energetic characteristics of adult and pediatric Sputnik left ventricular assist devices during mock circulation support. *Cardiology Research and Practice* **2019**, 4593174.
30. A. Quaini, S. Čanić, and D. Paniagua, Numerical charcterisation of haemodynamics conditions near aortic valve after implantation of left ventricular assist device. *Math. Biosci. Engrg.* **8** (2011), No. 3, 785–806.

31. P. Santagata, F. Rigo, S. Gherardi, L. Pratali, J. Drozdz, A. Varga, and E. Picano, Clinical and functional determinants of coronary flow reserve in non-ischemic dilated cardiomyopathy. *Int. J. Cardiology* **105** (2005), No. 1, 46–52.

32. A. Savitzky and M. J. E. Golay, Smoothing and differentiation of data by simplified least squares procedures. *Analytical Chemistry* **36** (2016), No. 8, 1627–1639.

33. R. F. Schmidt and G. Thews, *Human Physiology, Vol. 2*, 2nd ed. Springer-Verlag, Berlin–Heidelberg, Germany, 1989.

34. B. D. Seeley and D. F. Young, Effect of geometry on pressure losses across models of arterial stenoses. *J. Biomech.* (1976), No. 9, 439–448.

35. S. V. Selishchev and D. V. Telyshev, Optimisation of the Sputnik VAD design. *Int. J. Artificial Organs* **39** (2016), No. 8, 407.

36. Y. Shi, P. Lawford, and R. Hose, Review of zero-D and 1-D models of blood flow in the cardiovascular system. *Biomed. Engrg. OnLine* **10** (2011), 33. –414.

37. Y. Shi and T. Korakianitis, Impeller-pump model derived from conservation laws applied to the simulation of the cardiovascular system coupled to heart-assist pumps. *Computers in Biology and Medicine* **93** (2018), 127–138.

38. S. G. Shroff, J. S. Janicki, and K. T. Weber, Evidence and quantitation of left ventricular systolic resistance. *American J. of Physiology-Heart and Circulatory Physiology* **249** (1985), No. 2, H358–H370.

39. S. S. Simakov, Modern methods of mathematical modeling of blood flow using reduced order methods. *Computer Research and Modeling* **10** (2018), No. 5, 581–604.

40. S. Simakov and T. Gamilov, Computational study of the cerebral circulation accounting for the patient-specific anatomical features. *Smart Innovation, Systems and Technologies* **133** (2019), 309–330.

41. S. S. Simakov, Lumped parameter heart model with valve dynamics. *Russ. J. Numer. Anal. Math. Modeling* **34** (2019), No. 5, 289–300.

42. S. Simakov, A. Timofeev, T. Gamilov, Ph. Kopylov, D. Telishev, and Yu. Vassilevski, Analysis of operating modes for left ventricle assist devices via integrated models of blood circulation. *Mathematics* **8** (2020), No. 8, 1331.

43. H. Suga, Cardiac energetics: from E_{MAX} to pressure-volume area. *Clinical and Experimental Pharmacology and Physiology* **30** (2003), 580–585.

44. Y. Sun, B. J. Sjöberg, P. Ask, D. Loyd, and B. Wranne, Mathematical model that characterizes transmitral and pulmonary venous flow velocity patterns. *American J. of Physiology* **268** (1995), No. 1, H476–H489.

45. Y. Sun, M. Beshara, R. J. Lucariello, and S. A. Chiaramida, A comprehensive model for right-left heart interaction under the influence of pericardium and baroreflex. *American J. Physiology* **272** (1997), H1499–H1515.

46. D. Telyshev, M. Denisov, A. Pugovkin, S. Selishchev, and I. Nesterenko, The progress in the novel pediatric rotary blood pump sputnik development. *Artificial Organs* **42** (2018), No. 4, 432–443.

47. D. V. Telyshev, A. A. Pugovkin, and S. V. Selishchev, A mock circulatory system for testing pediatric rotary blood pumps. *Biomed. Engrg.* **51** (2017), No. 2, 83–87.

48. J. J. Teuteberg, J. C. Clevelend Jr, J. Cowge, et.al., The society of thoracic surgeons intermacs 2019 annual report: the changing landscape of devices and indications. *The Annals of Thoracic Surgery* **109** (2020), No. 3, 649-660.

49. D. Telyshev, D. Petukhov, and S. Selishchev, Numerical modeling of continuous-flow left

ventricular assist device performance. *Int. J. of Artificial Organs* **42** (2019), No. 11, 611–620.

50. F. N. Van de Vosse and N. Stergiopulos, Pulse wave propagation in the arterial tree. *Annual Rev. Fluid Mechanics* **43** (2011), 467–499.

51. Yu. Vassilevski, M. Olshanskii, S. Simakov, A. Kolobov, and A. Danilov, *Personalised Computational Haemodynamics: Models, Methods, and Applications for Vascular Surgery and Antitumor Therapy*. Academic Press, 2020.

52. Yu. V. Vassilevski, V. Yu. Salamatova, and S. S. Simakov, On the elasticity of blood vessels in one-dimensional problems of haemodynamics. *Comput. Math. Math. Phys.* **55** (2015), No. 9, 1567–1578.

53. Yu. V. Vassilevski, A. A. Danilov, S. S. Simakov, T. M. Gamilov, Yu. A. Ivanov, and R. A. Pryamonosov, Patient-specific anatomical models in human physiology. *Russ. J. Numer. Anal. Math. Modelling* **30** (2015), No. 3, 185–201.

54. K. R. Walley, Left ventricular function: time-varying elastance and left ventricular aortic coupling. *Critical Care* **20** (2016), No. 270, 1–11.

55. D. F. Young and F. Y. Tsai, Flow characteristics in models of arterial stenoses, I. Steady flow. *J. Biomechanics* (1973), No. 6, 395–410.

56. D. F. Young and F. Y. Tsai, Flow characteristics in models of arterial stenoses, II. Unsteady flow. *J. Biomechanics* (1973, No. 6, 547–559.

Appendix A

Tables A.1 and A.2 present the parameters of the systemic and coronary arteries, while Table A.3 contains the parameters of the Windkessel compartments.

Table A1. Parameters of the systemic arteries (see Fig. 2 for the vessels numbering).

No.	Artery title	Length (cm)	Radius (mm)	c_0 (cm/s)	mean RAF(%)
1a	Aortic arch Ip0	1.5	15.06	400	42.85
1b	Aortic arch Ip1	2.94	15.06	400	43.32
1c	Aortic arch Ip2	3.0	13.56	400	94.94
2	Brachiocephalic Trunk	4.74	6.44	440	13.96
3	Aortic arch II	0.96	12.76	410	80.98
4	Subclavian Right I	1.57	4.54	470	4.65
5	Common carotid right	8.12	3.9	500	9.31
6	Vertebral right	20.45	1.34	630	0.88
7a	Subclavian right II	4.11	3.24	520	3.76
7b	Axillary right	12.0	2.19	570	3.76
7c	Brachial right	22.31	1.95	580	3.76
8	Radial right	30.09	1.38	625	1.71
9	Ulnar right I	2.98	1.41	620	2.05
10a	Common interosseous right	1.63	0.96	660	0.36
10b	Posterior interosseous right	23.06	0.68	690	0.36
11	Ulnar right II	23.93	1.41	620	1.70
12	External carotid right	6.09	2.27	560	2.29
13	Internal carotid right	13.21	2.77	530	7.02
14	Common carotid left	12.13	3.9	490	9.21
15	Aortic arch III	0.7	12.42	410	71.77
16	External carotid left	6.09	2.27	560	2.28
17	Internal carotid left	13.21	2.77	530	6.93
18	Subclavian left I	4.94	4.19	480	4.64
19a	Aortic arch IV	4.31	11.42	410	67.13
19b	Thoracic aorta I	0.99	10.46	415	67.12
20	Vertebral left	20.42	1.34	630	0.88
21a	Subclavian left II	4.11	2.89	530	3.76

21b	Axillary left	12.0	2.19	570	3.76
21c	Brachial left	22.31	1.95	580	3.76
22	Radial left	31.09	1.38	625	1.73
23	Ulnar left I	2.98	1.41	620	2.02
24a	Common interosseous left	1.63	0.96	660	0.36
24b	Posterior interosseous left	23.06	0.68	690	0.36
25	Ulnar left II	23.93	1.41	620	1.67
26	Posterior intercostal T6 R	19.69	1.4	620	0.09
27	Thoracic aorta II	0.79	10.29	415	67.04
28	Posterior intercostal T6 left	17.8	1.4	622	0.08
29	Thoracic aorta III	1.56	10.07	415	66.95
30	Posterior intercostal T7 R	20.16	1.55	610	0.09
31	Thoracic aorta IV	0.53	9.87	415	66.86
32	Posterior intercostal T7 left	18.52	1.55	610	0.09
33a	Thoracic aorta V	12.16	8.68	420	66.76
33b	Thoracic aorta VI	0.32	7.52	430	66.76
34	Celiac trunk	1.68	3.28	510	10.99
35	Abdominal aorta I	1.4	7.41	430	55.77
36	Common hepatic	6.66	2.69	540	6.41
37	Splenic I	0.39	2.17	570	4.58
38	Left gastric	9.29	1.51	610	0.06
39	Splenic II	6.44	2.17	570	4.52
40	Superior mesenteric	21.64	3.93	490	9.85
41	Abdominal aorta II	0.43	7.29	430	45.92
42	Renal left	2.18	2.71	540	9.49
43	Abdominal aorta III	1.2	7.19	430	36.43
44	Renal right	3.77	3.1	520	9.47
45	Abdominal aorta IV	5.41	6.77	440	26.96
46	Inferior mesenteric	9.02	2.08	570	0.90
47	Abdominal aorta V	4.22	6.17	440	26.06
48	Common iliac right	7.64	4.29	480	13.04
49	Common iliac left	7.4	4.29	480	13.02
50a	External iliac right	10.22	3.28	510	7.86
50b	Femoral right I	3.16	3.17	515	7.86
51	Internal iliac right	7.25	2.82	530	5.18
52	Profunda femoris right	23.84	2.14	570	6.09
53a	Femoral right II	31.93	2.91	530	1.77
53b	Popliteal right I	13.2	2.53	550	1.76
54	Anterior tibial right	38.62	1.17	640	0.81
55a	Popliteal right II	0.88	2.36	555	0.95
55b	Tibiofibular trunk right	3.62	2.35	555	0.95
55c	Posterior tibial right	38.29	1.23	640	0.95
56a	External iliac left	10.22	3.28	510	7.85
56b	Femoral left I	3.16	3.17	515	7.85
57	Internal iliac left	7.25	2.82	530	5.16
58	Profunda femoris left	23.84	2.14	570	6.09
59a	Femoral left II	31.93	2.91	530	1.76
59b	Popliteal left I	13.2	2.53	550	1.76
60	Anterior tibial left	38.62	1.17	640	0.81
61a	Popliteal left II	0.88	2.36	555	0.95
61b	Tibiofibular trunk left	3.62	2.35	555	0.95
61c	Posterior tibial left	38.29	1.23	640	0.95
62	Basilar	2.6	1.75	700	1.76
63	Posterior cerebral right I	1.0	1.0	700	0.88
64	Posterior cerebral left I	1.0	1.0	700	0.88
65	Posterior cerebral right II	3.0	1.0	700	1.43
66	Posterior cerebral left II	3.0	1.0	700	1.42
67	Posterior communicating right	3.0	0.75	700	0.54
68	Posterior communicating left	3.0	0.75	700	0.54
69	Anterior cerebral left I	1.2	1.2	700	1.82
70	Anterior cerebral right I	1.2	1.2	700	1.89
71	Middle cerebral left	5.2	1.3	700	4.57
72	Middle cerebral right	4.3	1.25	700	4.58
73	Anterior cerebral right II	10.3	1.2	700	1.86

74	Anterior cerebral left II	10.3	1.2	700	1.86
75	Anterior communicating	0.3	0.75	700	0.03

Table A2. Parameters of the coronary arteries (see Fig. 3 for the vessels numbering).

No.	Artery title	Length (cm)	Radius (mm)	c_0 (cm/s)	R (kBa·s/ml)	mean RAF (%)
3	Left coronary artery root	2.61	2.48	1200	—	3.71
4	Left anterior descending I	1.83	2.07	1200	—	1.92
5		2.45	0.89	1200	—	0.39
6		0.65	0.45	1200	643.37	0.20
7		1.58	0.45	1200	643.37	0.19
8	Left anterior descending II	2.04	1.52	1200	—	1.53
9	Diagonal branch	2.76	0.98	1200	—	0.50
10		3.3	0.44	1200	505.08	0.22
11		1.98	0.48	1200	425.32	0.28
12	Left anterior descending III	1.32	1.16	1200	—	1.03
13		2.66	0.56	1200	305.91	0.39
14	Left anterior descending IV	3.67	0.89	1200	—	0.64
15		2.26	0.49	1200	405.88	0.29
16		1.94	0.53	1200	—	0.35
17		0.97	0.45	1200	643.37	0.18
18		1.84	0.45	1200	643.37	0.17
19	Left cirmcuflex I	3.13	1.96	1200	—	1.79
20	Left cirmcuflex II	4.97	1.45	1200	—	0.46
21		2.16	0.65	1200	449.28	0.28
22		4.05	0.92	1200	—	0.18
23		2.49	0.45	1200	$1.35{\cdot}10^3$	0.09
24		1.97	0.44	1200	$1.35{\cdot}10^3$	0.09
25	Left marginal branch	2.47	1.51	1200	—	1.32
26		2.45	0.89	1200	—	0.34
27		1.5	0.53	1200	714.04	0.18
28		1.11	0.52	1200	762.12	0.17
29		2.58	1.19	1200	—	0.98
30		1.34	0.54	1200	698.98	0.18
31		0.71	0.94	1200	—	0.80
32		2.1	0.51	1200	779.19	0.16
33		2.22	0.72	1200	—	0.64
34		1.23	0.45	1200	$5.84{\cdot}10^3$	0.02
35		0.71	0.94	1200	196.83	0.62
36	Right coronary artery root	1.74	1.73	1300	—	1.35
37		2.35	0.92	1300	—	0.12
38		0.38	0.45	1300	$2.20{\cdot}10^3$	0.06
39		0.27	0.44	1300	$2.20{\cdot}10^3$	0.06
40		2.05	0.98	1300	290.67	0.44
41	Right coronary I	2.42	1.63	1300	—	0.79
42		0.81	1.27	1300	—	0.25
43		1.86	0.78	1300	—	0.12
44		0.75	0.45	1300	$2.20{\cdot}10^3$	0.06
45		0.62	0.44	1300	$2.20{\cdot}10^3$	0.06
46		2.95	0.8	1300	—	0.13
47		0.47	0.46	1300	$1.68{\cdot}10^3$	0.08
48		0.76	0.46	1300	$2.20{\cdot}10^3$	0.06
49	Right coronary II	4.53	1.29	1300	—	0.54
50	Right marginal branch	1.84	0.99	1300	—	0.22
51		1.34	0.54	1300	$1.14{\cdot}10^3$	0.11
52		2.34	0.76	1300	—	0.11
53		3.17	0.36	1300	$2.20{\cdot}10^3$	0.05
54		1.05	0.27	1300	$2.20{\cdot}10^3$	0.05

55	Right coronary III	4.6	0.93	1300	—	0.32
56	Posterior descending	3.37	0.7	1300	—	0.11
57		2.34	0.3	1300	$2.20 \cdot 10^3$	0.05
58		1.88	0.34	1300	$2.20 \cdot 10^3$	0.05
59		2.42	0.75	1300	—	0.21
60		3.14	0.44	1300	$2.20 \cdot 10^3$	0.06
61		0.66	0.67	1300	—	0.15
62		1.47	0.45	1300	$2.20 \cdot 10^3$	0.06
63		0.87	0.58	1300	—	0.10
64		2.75	0.3	1300	$2.20 \cdot 10^3$	0.05
65		1.23	0.21	1300	$2.20 \cdot 10^3$	0.05

Table A3. Parameters of the Windkessel compartments (compartments numbering coincides with the terminal arteries numbering in Fig. 2).

No.	Artery title	R_1 (kBa·s/ml)	R_2 (kBa·s/ml)	C (ml/kBa)
8	Radial right	16.96	67.85	$4.91 \cdot 10^{-3}$
10b	Posterior interosseous right	70.28	281.14	$1.18 \cdot 10^{-3}$
11	Ulnar right II	17.27	69.08	$4.82 \cdot 10^{-3}$
12	External carotid right	13.8	55.22	$6.03 \cdot 10^{-3}$
16	External carotid left	13.85	55.41	$6.01 \cdot 10^{-3}$
22	Radial left	16.66	66.63	$5.00 \cdot 10^{-3}$
24b	Posterior interosseous left	70.54	282.16	$1.18 \cdot 10^{-3}$
25	Ulnar left II	17.6	70.42	$4.73 \cdot 10^{-3}$
26	Posterior intercostal T6 right	366.22	$1.46 \cdot 10^3$	$2.27 \cdot 10^{-4}$
28	Posterior intercostal T6 left	375.71	$1.50 \cdot 10^3$	$2.22 \cdot 10^{-4}$
30	Posterior intercostal T7 right	341.68	$1.37 \cdot 10^3$	$2.44 \cdot 10^{-4}$
32	Posterior intercostal T7 left	344.61	$1.38 \cdot 10^3$	$2.42 \cdot 10^{-4}$
36	Common hepatic	4.92	19.69	$1.69 \cdot 10^{-2}$
38	Left gastric	504.79	$2.02 \cdot 10^3$	$1.65 \cdot 10^{-4}$
39	Splenic II	6.96	27.83	$1.20 \cdot 10^{-2}$
40	Superior mesenteric	3.21	12.83	$2.60 \cdot 10^{-2}$
42	Renal left	3.33	13.3	$2.50 \cdot 10^{-2}$
44	Renal right	3.34	13.35	$2.49 \cdot 10^{-2}$
46	Inferior mesenteric	35.15	140.61	$2.37 \cdot 10^{-3}$
51	Internal iliac right	6.09	24.38	$1.37 \cdot 10^{-2}$
52	Profunda femoris right	5.04	20.15	$1.65 \cdot 10^{-2}$
54	Anterior tibial right	36.05	144.21	$2.31 \cdot 10^{-3}$
55c	Posterior tibial right	31.1	124.4	$2.68 \cdot 10^{-3}$
57	Internal iliac left	6.11	24.45	$1.36 \cdot 10^{-2}$
58	Profunda femoris left	5.04	20.16	$1.65 \cdot 10^{-2}$
60	Anterior tibial left	36.06	144.25	$2.31 \cdot 10^{-3}$
61c	Posterior tibial left	31.11	124.45	$2.68 \cdot 10^{-3}$
65	Posterior cerebral right II	21.11	84.44	$3.13 \cdot 10^{-3}$
66	Posterior cerebral left II	21.26	85.02	$2.94 \cdot 10^{-3}$
71	Middle cerebral left	6.38	26.37	$9.80 \cdot 10^{-3}$
72	Middle cerebral right	6.36	26.29	$9.83 \cdot 10^{-3}$
73	Anterior cerebral right II	16.16	64.62	$4.13 \cdot 10^{-3}$
74	Anterior cerebral left II	16.16	64.62	$4.13 \cdot 10^{-3}$